Fast-wave propagation and radio-frequency sheath interaction with a tokamak wall

H. Kohno[1,a)], J. R. Myra[2], and D. A. D'Ippolito[2]

[1]*Department of Mechanical Information Science and Technology, Kyushu Institute of Technology, 680-4 Kawazu, Iizuka, Fukuoka 820-8502, Japan*

[2]*Lodestar Research Corporation, 2400 Central Avenue P-5, Boulder, CO 80301, USA*

[a)] Electronic mail: kohno@mse.kyutech.ac.jp

Abstract

Interactions between propagating fast waves and radio-frequency (RF) sheaths in the ion cyclotron range of frequencies are numerically investigated based on a cold fluid plasma model coupled with a sheath boundary condition. In this two-dimensional study, the capability of the finite element code, which was developed in previous numerical work, is extended to analyze self-consistent RF sheath-plasma interaction problems in a tokamak with a non-circular cross-section. It is found that a large sheath voltage is generated near the edges of the limiter-shaped deformation as a result of the conversion from fast to slow waves on the sheaths. The sheath voltage associated with this conversion is particularly significant in the localized region where the contact angle between the magnetic field line and the conducting wall varies rapidly along the curved sheath surface, which is consistent with the results in previous one-dimensional theoretical work. The dependences of the RF sheaths on various parameters in plasma such as the toroidal wavenumber, the edge plasma density, and the degree of the RF wave absorption in the core region are also examined in detail.

PACS: 52.35.Mw, 52.40.Kh, 52.50.Qt, 52.55.Fa

I. INTRODUCTION

The efficient application of auxiliary power to fusion research plasmas is an important topic in contemporary research. The use of radio-frequency (RF) waves in the ion cyclotron range of frequencies (ICRF) for heating, current drive as well as other applications, has the advantage of being both cost effective and flexible. Indeed, ICRF heating is expected to play a significant role in the international tokamak experiment, ITER.[1]

While it is well recognized that ICRF wave coupling to the core plasma has been highly successful in many experiments, nevertheless, in certain regimes of operation, performance has been observed to be degraded due to edge and wall interactions. Reviews of experimental and theoretical work on ICRF edge and wall interactions are given in Refs. 2-3 and a short overview of the physics can be found in Ref. 4. More recently, these issues have been the subject of experimental investigations on many tokamaks,[5-13] and have given rise to a number of dedicated modeling efforts.[14-21] In particular, a large body of research has concentrated on the ubiquitous phenomenon of RF sheaths which form when plasma and RF waves coexist near material surfaces.

The fundamental mechanism for RF sheath formation is well understood.[2, 22-24] Electrons being more mobile than ions are more easily expelled from the plasma into the surface. A strong electric field builds up within a few Debye lengths of the wall to repel

electrons, attract ions, and maintain ambipolarity. The result is an RF sheath which can be responsible for power loss, impurity sputtering, and other unwanted interactions. Experimentally, RF sheaths have been observed both near the antenna and in more remote, "far field" locations. The voltage associated with these sheaths can often exceed thermal ($\sim 3T_e$ where T_e is the electron temperature) sheath levels by a large factor; RF sheaths of more than 100 V are not uncommon.

Among the modeling efforts, one line of investigations has concentrated on RF sheath interactions occurring with the antenna structure itself or with surfaces connected to the antenna by magnetic field lines.[6,14,15,19,22,25-28] In this case, the most important wave polarization component is $E_{\|}$ (the RF electric field component in the direction of the static, background magnetic field) associated with the slow wave (SW) (i.e., the electron plasma wave) branch. In these cases, models with slab-like geometry have proven useful for analysis; however, quantitative treatment of antenna interactions requires complex three-dimensional (3D) geometry, and is not the subject of the present paper.

A conceptually distinct situation, and the main topic of the present paper, occurs when a launched fast wave (FW) propagates either in the scrape-off layer (SOL)[13,16,29] or is weakly damped in the core and impacts the inner wall or perhaps another part of the vacuum vessel.[30] Although the FW does not itself have a significant $E_{\|}$ polarization, the boundary

conditions at the wall couple the FW and SW polarizations, as we shall see. This results in a SW component (which can be evanescent) near the wall and the appearance once again of RF sheaths.

There have been a number of modeling attempts of these FW far-field sheaths.[20,21,31,32] This past work has provided some useful insights and theoretical motivation for the present study. In particular, it was found that when field lines make an oblique intersection with the wall, boundary conditions on the FW electric field, which is essentially perpendicular to the background magnetic field, require the generation of $E_{\|}$. This can easily be seen, even for a metal wall for which the appropriate boundary condition is $\mathbf{E}_t = \mathbf{0}$ (where $\mathbf{E}_t$ refers to the electric field components tangential to the metal surface).

The wall-induced coupling of the FW and SW turns out to be rather general, and remains important when the full capacitive RF-sheath boundary condition[31,33] is employed. Consequently, the far-field sheath problem is fundamentally dependent on the wall geometry relative to the background magnetic field, the local FW polarization vector, and the tangential wave vector. The fact that previous modeling has made slab-like simplifications in the geometry motivates the present study. To our knowledge, it is the first work that employs all of the following: a global description of FW propagation in a model tokamak geometry, a wall shape that incorporates limiter-like deformations not conforming to flux surfaces, and the

capacitive sheath boundary condition (sheath BC). We shall see that all three of these features contribute to a deeper understanding of the far-field sheath process. In particular, the present paper will demonstrate explicitly the roles of wall geometry, FW propagation and cutoffs, strength of core ("single pass") absorption, and the nonlinearity of the sheath boundary condition. The latter effect, associated with the sheath-plasma resonance in previous work[18-21,32,33] here also can amplify the strength of RF sheaths.

The plan of our paper is as follows. In Sec. II we present the basic physics model for RF wave propagation and sheath interactions at the boundary. Section III introduces the model geometry (including wall, magnetic field, and plasma profiles) and the computational technique. This section goes on to discuss a computational base case which illustrates both direct magnetically connected and far-field sheaths. This is followed by further investigations which vary key parameters: wall shape, toroidal wavenumber (FW cutoff location), edge plasma density, and strength of core FW absorption. Finally, our conclusions are given in Sec. IV.

II. MODEL FOR SHEATH-PLASMA INTERACTIONS

In this section, we summarize the equations that govern the behavior of plasma waves

and the interaction between the ICRF waves and the sheaths on metal surfaces. In the following analysis, we assume that deuterium is the only ion species; however, the formalism is easily generalized to different or multiple species by appropriate modifications to the dielectric tensor.

The governing equation for plasma waves is a combined form of Maxwell's equations described as

$$\nabla \times \nabla \times \mathbf{E} - \frac{\omega^2}{c^2} \boldsymbol{\varepsilon} \cdot \mathbf{E} - \mathrm{i}\omega\mu_0 \mathbf{J}_{\mathrm{ext}} = \mathbf{0}, \tag{1}$$

where the electric field $\mathbf{E}$ and the external current $\mathbf{J}_{\mathrm{ext}}$ vary on the RF time scale. Here, ω is the applied ICRF wave frequency, c is the speed of light, i is the imaginary unit, and μ_0 is the permeability in vacuum. The dielectric tensor $\boldsymbol{\varepsilon}$ is given by the cold plasma model.[34] Throughout this study, we assume that quasi-neutrality in the plasma is retained, i.e., $n_{\mathrm{e}} = n_{\mathrm{i}}$ where n_{e} and n_{i} are the equilibrium electron and ion densities, respectively.

At the metal wall, the sheath effect is taken into account by means of a capacitive sheath BC[31,33], which is written as follows:

$$\mathbf{E}_{\mathrm{t}} = \nabla_{\mathrm{t}} \left(\frac{\Delta_{\mathrm{sh}}}{\varepsilon_{\mathrm{sh}}} D_{\mathrm{n}} \right). \tag{2}$$

Here, Δ_{sh} is the time-averaged sheath width, $\varepsilon_{\mathrm{sh}}$ is the dielectric constant in the sheath (in this study we assume that $\varepsilon_{\mathrm{sh}} = \varepsilon_0$, where ε_0 is the dielectric constant in vacuum), $D_{\mathrm{n}} \left(= \varepsilon_0 \mathbf{s} \cdot \boldsymbol{\varepsilon} \cdot \mathbf{E} \right)$ is the component of the electric displacement normal to the sheath (and $\mathbf{s}$ is

the unit normal vector pointing into the plasma), and the subscript t denotes the two components tangential to the boundary. In a manner consistent with the Child-Langmuir law,[35,36] the sheath width is written as follows:

$$\Delta_{\mathrm{sh}} = \left(\frac{eC_{\mathrm{sh}}}{\varepsilon_{\mathrm{sh}} T_{\mathrm{e}}} \left| D_{\mathrm{n}} \right| \right)^3 \lambda_{\mathrm{De}}^4 + C_{\mathrm{th}} \lambda_{\mathrm{De}}, \tag{3}$$

where e is the electric charge, C_{sh} is an order-unity constant giving the rectification factor (which is fixed at 0.6 in this study), T_{e} is the electron temperature, and λ_{De} is the electron Debye length defined as $\lambda_{\mathrm{De}} = \left(\varepsilon_0 T_{\mathrm{e}} / n_{\mathrm{e}} e^2 \right)^{1/2}$. The first and second terms on the right-hand side of Eq. (3) are the RF and thermal sheath contributions to the self-consistent sheath width, respectively. The coefficient C_{th} has different forms depending on whether the contact angle between the magnetic field line and the wall (hereafter, this is simply called the contact angle) is smaller (ion poor sheath) or larger (electron poor sheath) than a critical value. Using a polynomial fit to transition smoothly between the two limits, C_{th} is given by

$$C_{\mathrm{th}}\left(\left| b_{\mathrm{n}} \right| \right) = \begin{cases} a_1 \left| b_{\mathrm{n}} \right|^4 + a_2 \left| b_{\mathrm{n}} \right|^3 & \text{for } \left| b_{\mathrm{n}} \right| \le b_{\mathrm{crit}} \\ \left\{ \ln\left[\left(\dfrac{m_{\mathrm{i}}}{m_{\mathrm{e}}} \right)^{1/2} \left| b_{\mathrm{n}} \right| \right] \right\}^{3/4} & \text{for } \left| b_{\mathrm{n}} \right| > b_{\mathrm{crit}}, \end{cases} \tag{4}$$

where m_{i} and m_{e} are the ion mass and electron mass, respectively, and b_{n} is defined by $b_{\mathrm{n}} = B_{0\mathrm{n}} / \left| \mathbf{B}_0 \right|$ (a component of $\mathbf{b} = \mathbf{B}_0 / \left| \mathbf{B}_0 \right|$) where $\mathbf{B}_0$ is the background magnetic field and $B_{0\mathrm{n}}$ is its component normal to the sheath. The coefficients a_1 and a_2 are determined so as to satisfy the continuity of C_{th} and $\mathrm{d}C_{\mathrm{th}} / \mathrm{d}\left| b_{\mathrm{n}} \right|$ at $\left| b_{\mathrm{n}} \right| = b_{\mathrm{crit}}$, where $b_{\mathrm{crit}} \approx \left(m_{\mathrm{e}} / m_{\mathrm{i}} \right)^{1/2}$. Since

we assume a deuterium plasma, the value of b_{crit} is fixed at 0.02 in this study. We note that Eq. (3) is strictly valid for $eV_{\mathrm{sh}}/T_{\mathrm{e}} >> 1$ and $eV_{\mathrm{sh}}/T_{\mathrm{e}} << 1$, where V_{sh} is the instantaneous RF sheath voltage defined by

$$V_{\mathrm{sh}} = \Delta_{\mathrm{sh}} \left| E_{\mathrm{n}}^{(\mathrm{sh})} \right| = \Delta_{\mathrm{sh}} \left| \frac{D_{\mathrm{n}}^{(\mathrm{pl})}}{\varepsilon_{\mathrm{sh}}} \right|, \tag{5}$$

with the superscripts sh and pl denoting the quantities on the sheath and plasma sides of the sheath-plasma interface, respectively. In intermediate cases, $eV_{\mathrm{sh}}/T_{\mathrm{e}} \sim 1$, Eq. (3) provides a smooth and approximate interpolation.

In the present work, we consider RF sheaths arising from the interaction of FWs with a model limiter surface. We assume that the FWs that enter the core plasma are weakly damped there. In order to assure this in the framework of the cold plasma model, we introduce a simple ad-hoc friction in the plasma volume similar to the absorbing boundary condition approach used in the previous slab model.[19] This approach consists of defining the ion mass as $\hat{m}_{\mathrm{i}} = m_{\mathrm{i}}\left(1 + \mathrm{i}\nu_{\mathrm{i}}/\omega\right)$ and choosing the artificial collision frequency ν_{i} to decrease exponentially from the core plasma so as to simulate core absorption processes. (As discussed in Appendix A, complex ion, rather than electron, mass is required to damp the FW). In this study, ν_{i} is described in the following equation:

$$\nu_{\mathrm{i}} = \nu_{\mathrm{i}0} \exp\left(-\frac{\rho^2}{\lambda_\nu^2} \right), \tag{6}$$

where $\nu_{\mathrm{i}0}$ is the maximum artificial frequency, ρ is the distance from the center of the core

plasma (defined more specifically later), and λ_v represents the damping length. Although we do not show it explicitly in this paper, the complex ion mass plays an important role in eliminating eigenmode sensitivity of calculated FWs in a closed domain.

The combined form of Maxwell's equations and the sheath BC are self-consistently solved with the rfSOL code, which is based on a finite element method as presented in Ref. 37. The rfSOL code has undergone significant upgrades from the previous versions (applied to a singly periodic slab model) in order to accurately calculate sheath-plasma interactions on general curvilinear geometry. The key upgrades are summarized in Appendix B. The calculations in this paper were performed on the Hopper Cray XE6 computer system at the National Energy Research Scientific Computing Center (NERSC).

III. NUMERICAL SIMULATION OF FW-SHEATH INTERACTIONS

In our previous work, we have analyzed various two-dimensional sheath-plasma interaction problems in a singly periodic slab model.[19,21] In the present numerical analysis, we consider sheath-plasma interactions, in particular FW-sheath interactions, with a spatially varying background magnetic field and spatially varying plasma densities in a small high-field tokamak. The default parameters used in the analysis are similar to those of Alcator

C-Mod, but instead of modeling the full X-point divertor geometry, we employ a circular cross-section geometry. In addition, we incorporate a limiter-shaped deformation, which is called "limiter protrusion" hereafter, from a circular wall in a particular range of poloidal angles in the model. The magnetic field geometry is that of a "cylindrical tokamak," i.e., no toroidal effects are modeled; instead, it is as if the torus were cut at a particular toroidal angle and rolled out into a cylinder which is periodic along z, the axis of the cylinder.

Figure 1(a) shows the problem definition which corresponds to an approximated geometry of the plasma region including an antenna in the poloidal cross-section of a tokamak. Here, the radius of the quasi-circular domain, a, and the antenna length l_{ant} are fixed at 0.3 m and 0.4 m, respectively, which correspond to the minor radius and antenna length of the Alcator C-Mod tokamak. The origin in the Cartesian coordinate system is placed at the center of the domain, and the poloidal angle θ is defined such that $\theta = 0$ on the positive x-axis and its value is increased in the counterclockwise direction. It is assumed that the antenna is located at the radius $r_{\text{ant}} = 0.25$ m with its center position on the positive x-axis. The local height of the limiter protrusion, δa, is given by the following equation:

$$\delta a(\theta) = h_{\text{p}}\left[\frac{1}{2}\left(1+\tanh\frac{\theta-\theta_{\text{on}}}{\Delta\theta_{\text{slope}}}\right)-\frac{1}{2}\left(1+\tanh\frac{\theta-\theta_{\text{off}}}{\Delta\theta_{\text{slope}}}\right)\right], \tag{7}$$

where h_{p} is the maximum height of the protrusion, θ_{on} and θ_{off} are the poloidal angles at the edges of the protrusion ($\theta_{\text{on}} < \theta_{\text{off}}$), and $\Delta\theta_{\text{slope}}$ is the angle which determines the edge

slopes of the protrusion. In the present analysis, the three angles are determined such that $\theta_{\text{on}} = 160\pi/180$, $\theta_{\text{off}} = 200\pi/180$, and $\Delta\theta_{\text{slope}} = 1.2\pi/180$. Note that in the present model the limiter protrusion is located on the inner side of the torus to investigate the interactions of the protrusion with a propagating FW. While tokamaks sometimes operate in an inner-wall limited configuration, actual protrusions are usually on the outboard side of the torus. We avoid this geometry in order to cleanly separate the role of FW sheaths from direct magnetically connected sheaths.

For calculations we use the mesh as shown in Fig. 1(b), which consists of nine-node elements; here, a quadrilateral in the mesh corresponds to a nine-node element. As will be seen in the numerical results, extreme care must be exercised to accurately resolve the fine-scale structures near the poloidal edges of the limiter protrusion. For this purpose, the radial and circumferential grid resolutions are adjusted in a manner such that sufficiently fine resolution is secured near the edges of the deformation. Specifically, the grid points in the ranges of $r_{\text{ant}} < r \le a - \delta a$ and $0 < \theta \le \pi$ are distributed in the radial and circumferential directions according to the following equations:

$$r(i) = \begin{cases} r_{\text{ant}} + \dfrac{\mathrm{e}^{\alpha_r (2i/N_r)} - 1}{2\left(\mathrm{e}^{\alpha_r} - 1\right)}\left(a - \delta a - r_{\text{ant}}\right) & \text{for } 1 \le i \le N_r/2 \\ r_{\text{ant}} + \left\{1 - \dfrac{\mathrm{e}^{\alpha_r [1 - 2(i - N_r/2)/N_r]} - 1}{2\left(\mathrm{e}^{\alpha_r} - 1\right)}\right\}\left(a - \delta a - r_{\text{ant}}\right) & \text{for } N_r/2 + 1 \le i \le N_r, \end{cases} \tag{8}$$

$$\theta(i)=\begin{cases}\left[1-\dfrac{\mathrm{e}^{\alpha_{\theta 1}(1-i/N_{\theta 1})}-1}{\mathrm{e}^{\alpha_{\theta 1}}-1}\right]\theta_{\mathrm{on}} & \text{for } 1\le i\le N_{\theta 1};\ 0<\theta\le\theta_{\mathrm{on}} \\ \theta_{\mathrm{on}}+\dfrac{\mathrm{e}^{\alpha_{\theta 2}(i/N_{\theta 2})}-1}{\mathrm{e}^{\alpha_{\theta 2}}-1}(\pi-\theta_{\mathrm{on}}) & \text{for } 1\le i\le N_{\theta 2};\ \theta_{\mathrm{on}}<\theta\le\pi, \end{cases} \tag{9}$$

where N_r is the number of elements included in the radial direction in the range of $r_{\mathrm{ant}} \le r \le a-\delta a$, and $N_{\theta 1}$ and $N_{\theta 2}$ are the numbers of elements included in the circumferential direction in the ranges of $0\le\theta\le\theta_{\mathrm{on}}$ and $\theta_{\mathrm{on}}\le\theta\le\pi$, respectively. Using Eqs. (8) and (9), one can achieve very high accuracy near the edge of the limiter only by increasing the values of the uneven parameters α_r, $\alpha_{\theta 1}$, and $\alpha_{\theta 2}$. The grid points in the ranges of $r_{\mathrm{ant}} < r \le a-\delta a$ and $\pi<\theta\le 2\pi$ can also be distributed in a similar way, since we assume up-down symmetry in the geometry with respect to the x-axis. The grid distribution in the domain of $r\le r_{\mathrm{ant}}$ is not very important (i.e., accuracy is not sensitive to the grid distribution in this range) for the present finite element analysis.

The electric field in the whole domain is solved subject to the sheath BC on the entire boundary. The antenna surface current is given by a trigonometric function in the poloidal direction as follows:

$$\mathbf{J}_{\mathrm{ext}} = K(u)\,\delta(r-r_{\mathrm{ant}})\,\mathrm{e}^{\mathrm{i}(k_z z-\omega t)}\mathbf{e}_\theta, \tag{10}$$

with

$$K(u)=K_{\max}\sin^2\frac{\pi u}{l_{\mathrm{ant}}}, \tag{11}$$

where u is the coordinate along the antenna on the x-y plane; $u=0$ at the end of the

antenna in $y<0$. Thus, the antenna current is maximum at the center of the antenna and zero at the two ends. In Eq. (10), k_z is the toroidal wavenumber, $\mathbf{e}_\theta$ is the unit vector in the θ direction (the same shall apply to $\mathbf{e}_x$, $\mathbf{e}_y$, and $\mathbf{e}_z$), and $K_{\max}$ is the maximum antenna current density. The spatially varying background magnetic field is given by

$$\mathbf{B}_0 = B_{0z}\mathbf{e}_z + \mathbf{e}_z \times \nabla \Psi_{\mathrm{p}}, \tag{12}$$

with

$$\begin{aligned} &\Psi_{\mathrm{p}} = \frac{B_{0z}}{R}\int_0^{\rho} \frac{\widetilde{\rho}}{q(\widetilde{\rho})}\mathrm{d}\widetilde{\rho}, \\ &q(\rho) = q_0 + (q_a - q_0)\frac{\rho^2}{a^2}, \\ &\rho = |\mathbf{r} - \mathbf{r}_0|, \quad \mathbf{r} = (x, y), \quad \mathbf{r}_0 = (x_0, y_0), \end{aligned} \tag{13}$$

where R and q denote the major radius of the tokamak and the safety factor, respectively; here, q_0 and q_a correspond to the safety factors at $\rho = 0$ and $\rho = a$, respectively. It can be easily checked that the above expression satisfies $\nabla \cdot \mathbf{B}_0 = 0$ for constant B_{0z}. In addition, we assume that the electron density profile is expressed as

$$n_{\mathrm{e}} = \left(n_{\mathrm{e}}\big|_{\Psi_{\mathrm{p}}=0} - n_{\mathrm{e}}\big|_{\Psi_{\mathrm{p}}=\infty} \right) \mathrm{sech}\left[\left(\frac{\rho}{\lambda_n} \right)^{\nu} \right] + n_{\mathrm{e}}\big|_{\Psi_{\mathrm{p}}=\infty}, \tag{14}$$

where $n_{\mathrm{e}}\big|_{\Psi_{\mathrm{p}}=0}$ and $n_{\mathrm{e}}\big|_{\Psi_{\mathrm{p}}=\infty}$ are the electron densities at $\Psi_{\mathrm{p}} = 0$ ($\mathbf{r} = \mathbf{r}_0$) and $\Psi_{\mathrm{p}} = \infty$ (approximately on the boundary of the domain for $a - \delta a >> \lambda_n$), respectively. Note that the magnetic axis, $\rho = 0$, is displaced from the geometric center of the circular part of the wall when $\mathbf{r}_0 \neq \mathbf{0}$. This permits *some* field lines to make a direct magnetic connection between the

antenna and the wall; and also permits a finite thickness SOL of open field lines, even in the absence of a limiter protrusion.

All the calculations in this study will be conducted with a nonlinear sheath BC, in which the electric field contribution to the sheath width (i.e., the first term in Eq. (3)) is included. Together with the geometry parameters already described above, we fix the following parameters in all the cases: $N_r = 48$, $N_{\theta 1} = 398$, $N_{\theta 2} = 50$, $\alpha_r = 2$, and $\alpha_{\theta 1} = \alpha_{\theta 2} = 4$ for the mesh which includes 157696 nine-node elements (note that Fig. 1(b) includes only 1476 nine-node elements to display the grid arrangement clearly); $K_{\max} = 3\,\mathrm{kA/m}$ for the antenna surface current; $B_{0z} = 4\,\mathrm{T}$, $R = 0.6\,\mathrm{m}$, $q_0 = 1$, $q_a = 1.1$, $x_0 = -0.04\,\mathrm{m}$, and $y_0 = 0\,\mathrm{m}$ for the background magnetic field; $n_\mathrm{e}\big|_{\Psi_\mathrm{p}=0} = 10^{20}\,\mathrm{m}^{-3}$, $\lambda_n = 0.15\,\mathrm{m}$, and $\nu = 4$ for the electron density; $\lambda_\nu = 0.05\,\mathrm{m}$ for the FW damping in the core; $T_\mathrm{e} = 10\,\mathrm{eV}$ and $f = 80\,\mathrm{MHz}$ where $\omega = 2\pi f$. The other parameters which have not yet been specified are varied in the present numerical analysis.

As an example, the electron density profile for $n_\mathrm{e}\big|_{\Psi_\mathrm{p}=\infty} = 10^{18}\,\mathrm{m}^{-3}$ is shown in Fig. 2. The parameters used in this study correspond roughly to typical Alcator C-Mod parameters, except for q_a. The relatively small value of q_a used here enhances the angle that the background magnetic field makes with the vessel surface and results in larger $|b_\mathrm{n}|$ and stronger sheath interactions. In a real tokamak, large angles (up to $\pi/2$) would result from

poloidal limiters and other hardware which protrude into the torus at particular toroidal locations. Detailed modeling of such structures, which requires a 3D treatment, is beyond the capability of the present code.

A. Base case

First of all, the characteristic FW-sheath interactions in the presence of the limiter protrusion are investigated by employing a set of parameters referred to as the base case. Together with the fixed parameters, the maximum height of the protrusion, the toroidal wavenumber, the edge electron density, and the maximum artificial frequency are determined such that $h_{\mathrm{p}} = 0.03\,\mathrm{m}$, $k_z = 2.7\,\mathrm{m}^{-1}$, $n_{\mathrm{e}}\big|_{\Psi_{\mathrm{p}}=\infty} = 10^{18}\,\mathrm{m}^{-3}$, and $\nu_{\mathrm{i}0} = 0.2\omega$ for the base case. The filled contour plots of the real part of the electric field components perpendicular and parallel to the background magnetic field, which are defined by $E_{\perp y} = \left(\mathbf{E} - E_{\parallel}\mathbf{b}\right)\cdot\mathbf{e}_y$ and $E_{\parallel} = \mathbf{E}\cdot\mathbf{b}$, respectively, are shown in Fig. 3. Here, the antenna and magnetic field lines are also superimposed on the plots. Figure 3 shows (i) a propagating FW impacting the limiter protrusion (see Fig. 3(a)); (ii) near field generated $E_{\parallel}$ which follows the magnetic field lines and can potentially create direct magnetically connected sheaths (see Fig. 3(b)); and (iii) $E_{\parallel}$ generated by the FW-to-SW conversion near the edge of the protrusion (see Fig. 3(c)), by the process discussed in the introduction. For the given parameters, the analysis using the local

dispersion relation shows that the FW propagates across the plasma (from right to left on the poloidal cross-section) with a small amount of attenuation, which is slightly visible in Fig. 3(a). Note that the emergence of the large parallel electric field component near the edge of the limiter protrusion is a separate phenomenon unrelated to the direct magnetic connection between the antenna and the conducting wall. Therefore, it should be emphasized that the present numerical analysis reveals two distinct types of RF sheaths: the direct magnetically connected sheaths and the sheaths due to the FW-to-SW conversion. By construction of the simulation, these sheaths are well separated spatially. The latter type of sheath is enhanced by rapid tangential variation of the contact angle $|b_n|$, as will be demonstrated later, which was analytically predicted by a one-dimensional (1D) model.[20,32] In the present work, we focus particularly on this type of sheath and investigate how the instantaneous RF sheath voltage on the limiter edges varies depending on the parameters which are not fixed in this numerical analysis. In the following analyses, we consider varying only one parameter for each case keeping all the other parameters the same as in the base case.

B. Dependence on wall shape

Next, the dependence of the sheath on the contact angle is investigated by varying only the maximum height of the limiter protrusion from the base case parameters. Here, we consider four different values of h_{p}: 0 m, 0.01 m, 0.02 m, and 0.03 m (the base case). Figure

4 shows the variations of the instantaneous RF sheath voltage along the sheath surface for the four different values of h_{p}. It is seen in Fig. 4(a) that the sheath voltage abruptly increases near the poloidal angles of 160 and 200 degrees for the cases where h_{p} is nonzero. As described just after Eq. (7), these poloidal angles correspond to the locations of the edge slopes of the limiter protrusion. More detailed information about the small-scale variations around 160 degrees can be seen in Fig. 4(b), which shows the variations only in a limited range of the poloidal angle. From this figure, it is found that the sheath voltage is approximately proportional to the protrusion height which controls the contact angle $|b_n|$ (as will be confirmed in Fig. 5). Indeed, this is related to the FW-to-SW conversion observed in Fig. 3(c); a SW is generated in the process that a propagating FW interacts with conducting surfaces having small-scale length features. The magnitude of the sheath voltage depends on the contact angle and the rate of change of that angle along the sheath surface. Again, these results are consistent with earlier 1D work.[20,32] On the other hand, direct magnetically connected sheaths near 90 and 270 degrees likely give rise to the "plateau" of the sheath voltage (see Figs. 3(b) and 4(a)).

Figure 5 shows the variations of the real part of $E_{\perp y}$ and $|b_{\mathrm{n}}|$ along the sheath surface with enlargement for the limiter region; the profiles of these two quantities are compared for the case with $h_{\mathrm{p}} = 0\,\mathrm{m}$ and the case with $h_{\mathrm{p}} = 0.03\,\mathrm{m}$ (i.e., the base case).

These plots show that (i) the field strength of the incoming FW in the absence of the limiter protrusion is a few kV/m as a whole (see Fig. 5(a)); (ii) the presence of the limiter protrusion dramatically increases both $\mathrm{Re}(E_{\perp y})$ and $|b_{\mathrm{n}}|$ (see Fig. 5(b)); and (iii) the sheath due to the FW-to-SW conversion is formed where $|b_{\mathrm{n}}|$ changes rapidly (also, see Fig. 5(b)). The point (iii) above is associated with the distribution of $E_{\|}$ near the edge of the limiter protrusion in Fig. 3(c); although not shown here, the maximum value of $\mathrm{Re}(E_{\|})$ in the range of $140° \le \theta \le 220°$ for $h_{\mathrm{p}} = 0\,\mathrm{m}$ is about 0.4 kV/m, while the maximum value of $\mathrm{Re}(E_{\|})$ in the same range for $h_{\mathrm{p}} = 0.03\,\mathrm{m}$ is about 2.2 kV/m at $\theta = 164°$. Thus, some of the $E_{\perp y}$ increase in the presence of the limiter protrusion could be due to the SW that is generated. The electric field strength shown in these figures is similar to that for the Alcator C-Mod experiment (i.e., $E_{\perp}$ is on the order of a few kV/m), and the computed sheath voltage is similar to the experimental measurements (100 V or more).[13] In addition, these numerical results confirm earlier 1D modeling which could only represent the limiter protrusion using an effective k-vector along the sheath surface.[20]

C. Dependence on k_z

To investigate the dependence of the sheath on k_z, calculations are performed with only the value of k_z varied from the base case parameters. Here, we consider four different

values of k_z: $2.7\,\mathrm{m}^{-1}$ (the base case), $5.4\,\mathrm{m}^{-1}$, $8.1\,\mathrm{m}^{-1}$, and $10.8\,\mathrm{m}^{-1}$. Figure 6 shows the variations of the instantaneous RF sheath voltage along the sheath surface for the four different values of k_z. It is seen that the sheath voltage dramatically reduces for large values of k_z. This is consistent with smaller electric fields present in the boundary, which is confirmed in Fig. 7 showing the filled contour plot of the real part of $E_{\perp y}$ for $k_z = 10.8\,\mathrm{m}^{-1}$. Here, a blue, closed curve, which denotes the locations where a cutoff of the FW occurs, is also superimposed on the plot. Compared to the corresponding plot for the base case (shown in Fig. 3(a)), it is evident for $k_z = 10.8\,\mathrm{m}^{-1}$ that the FW is evanescent in the edge of the domain and does not reach the limiter protrusion. In fact, reduced sheath power dissipation and impurity production are frequently observed experimentally as k_z is increased.[29,38-41]

The FW cutoff condition relevant in this analysis (i.e., for $n_{\|}^2 > 1$) is given by

$$1 + \frac{\omega_{\mathrm{pi}}^2}{\Omega_{\mathrm{i}}\left(\omega + \Omega_{\mathrm{i}}\right)} = \frac{c^2 k_{\|}^2}{\omega^2}, \tag{15}$$

where ω_{pi} is the ion plasma frequency, and Ω_{i} is the ion cyclotron frequency (see Appendix A for details). We can evaluate this condition in a slab model, approximating the component of $\mathbf{k}$, the wave vector, in the poloidal direction by $\pm\pi/l_{\mathrm{ant}}$ and taking the edge magnetic field in the poloidal direction as $B_{\mathrm{p}} \approx aB_z/q_a R$. In this approximation, we find that the FW in the base case ($k_z = 2.7\,\mathrm{m}^{-1}$) has one branch that is not cut off while for the enhanced k_z case ($k_z = 10.8\,\mathrm{m}^{-1}$) all branches ($k_{\mathrm{p}} = \pm\pi/l_{\mathrm{ant}}$) of the FW are cut off for

$n_i = n_e < 2.7\times10^{18}$ m^{-3}. This explains the difference in the wave propagation in the boundary.

Based on the cutoff expression, we note that similar cutoff modifications can be achieved by changing the plasma density and the background magnetic field. Such examples will not be shown explicitly in this paper for reasons of brevity. The importance of the cutoff condition for FW propagation in the boundary region has been noted in a series of experimental and theoretical papers on NSTX.[11,16,29] In particular, recent modeling of wave propagation using the AORSA code suggests strong boundary interaction and power loss in the case where the FW propagates in the SOL.[16] In that work, sheath BCs were not employed, and power loss was modeling by artificial dissipation. Here we extend that treatment (in a simplified RF wave and geometry model) to include explicitly the FW-to-SW conversion effect and the resulting sheath interactions.

D. Dependence on plasma density

In order to assess potential SW-sheath interactions, the dependence of the sheath on the edge plasma density is investigated by varying only the edge electron density $n_e|_{\Psi_p=\infty}$ from the base case parameters. Here, we consider four different values of $n_e|_{\Psi_p=\infty}$: 4×10^{17} m^{-3}, 6×10^{17} m^{-3}, 8×10^{17} m^{-3}, and 10^{18} m^{-3} (the base case). Figure 8(a) shows the variations of the instantaneous RF sheath voltage along the sheath surface for the four

different values of $n_e|_{\Psi_p=\infty}$ (note that n_e in the legend of the graph means $n_e|_{\Psi_p=\infty}$ to be precise). Also, Fig. 8(b) shows the filled contour plot of the real part of $E_\parallel$ for $n_e|_{\Psi_p=\infty} = 4\times10^{17}$ m^{-3}. From these plots, it is noticed that the direct magnetically connected sheaths are enhanced in the boundary region for the low edge plasma density; even though there are no small-scale variations along the sheath surface, the direct magnetically connected sheaths yield the sheath voltage of more than 300 V for $n_e|_{\Psi_p=\infty} = 4\times10^{17}$ m^{-3}. Thus, for these parameters the SW-sheath interaction is much stronger than the FW-sheath interaction. Considering that the FW-sheath interaction is noticeable only when the FW-to-"SW" conversion occurs in the present numerical analysis, having sufficiently small $E_\parallel$ on the sheath is an important requirement to make the RF sheath voltage small. Recall that the sheath width and self-consistent sheath voltage in Eqs. (3) and (5) depend strongly on $D_n = \varepsilon_0\varepsilon_\parallel E_\parallel \mathbf{s}\cdot\mathbf{b}$ in general since a relative ordering of the dielectric tensor components is $|\varepsilon_\parallel| >> |\varepsilon_\perp|,\ |\varepsilon_\times|$ (see Ref. 34).

To better understand the results in Fig. 8, it is necessary to examine the properties of the SW under the given conditions; specifically, we need to calculate the evanescence rate along the magnetic field lines on the cross-section for specified k_z. To achieve this, let us temporarily define ξ and η coordinates such that ξ and η are perpendicular to and along the magnetic flux surfaces, respectively in the x-y plane. Then, a rough estimate for

k_ξ (the wave vector component in the ξ direction described above; the same shall apply to k_η later) is $k_\xi = \pi / l_\xi$ where l_ξ is the radial scale length of the $E_\parallel$ structure measured from Fig. 8(b), which is estimated as $l_\xi = 0.02$ m. The SW dispersion relation is

$$n_\parallel^2 = \varepsilon_\perp \left(1 - \frac{n_\perp^2}{\varepsilon_\parallel} \right) \tag{16}$$

(where $n_\perp^2 = n^2 - n_\parallel^2$; see Appendix A for the definitions of n^2 and $n_\parallel^2$) and then using $k_\parallel = b_\eta k_\eta + b_z k_z$ (where $b_\eta \approx B_\mathrm{p} / B_z$ and $b_z \approx \left(1 - b_\eta^2\right)^{1/2}$); see subsection C), one can solve for k_η. Using base case parameters, except for the plasma density n_e which is varied, it is found that the plasma density at which the value of $\mathrm{Im}\left(k_\eta\right)$ starts to grow is close to the lower hybrid plasma density, $n_\mathrm{e} = 2.5 \times 10^{17}$ m^{-3}, obtained by simply assuming $\varepsilon_\perp = 0$ in a slab model. For the range of edge plasma densities illustrated, there is no SW propagation in the boundary region but there is always FW propagation (again, see subsection C). On the other hand, although the SW fields are evanescent, the rate of evanescence is reduced at low plasma density as the lower hybrid resonance density is approached, enhancing the direct magnetically connected sheaths as seen in Fig. 8(a).

In Fig. 8(b), a relatively large $E_\parallel$ due to the FW-to-SW conversion, which is associated with the sheath voltage of 200 V around $\theta = 160°$ in Fig. 8(a), is also observed near the edge of the limiter protrusion. Therefore, the present calculation illustrates that *two types of sheaths can be present in the same experiment and can show different dependencies*

on parameters – not only plasma parameters but also geometric and antenna design parameters. A recent comprehensive study[13] of the plasma potential distribution on Alcator C-Mod supports this picture of having multiple types of sheaths simultaneously in the same experiment. This can complicate the experimental diagnosis and optimization of RF performance.

E. Dependence on central absorption

Lastly, the dependence of the sheath on the central absorption (i.e., absorption in the core plasma) is investigated by varying only the maximum artificial frequency ν_{i0} from its base case value. Here, we compare the results using two different values of ν_{i0}: 0.2ω (the base case) and 0.4ω. Figure 9 shows the comparison of the variations of the instantaneous RF sheath voltage and the real part of $E_{\perp y}$ along the sheath surface for the two cases. It is seen, as expected, that stronger central absorption (with increased ν_{i0}) reduces the sheath voltage at the edge of the limiter protrusion and the electric field on the boundary. This result is good for ICRF operation in the full field ITER experiments where central absorption is expected to be excellent. However, it should be noted that the significant interactions between the RF waves and the conducting wall may occur in the start-up phase of ITER (with magnetic field reduced by half) where the central absorption is expected to be poor. The

increase of RF edge interactions in cases of poor single pass absorption has been seen in experiments.[2,24,30] From the plots shown in Fig. 9, it is noticed that the sheath voltage V_{sh} changes by a larger factor compared to the electric field $\mathrm{Re}\left(E_{\perp y}\right)$ when the maximum artificial frequency is reduced from 0.4ω to 0.2ω. This is due to the nonlinear dependence of V_{sh} on D_{n} (see Eqs. (3) and (5)).

The nonlinearity referred to in the preceding discussion has been seen in other studies to play an important role in RF-sheath interactions. In particular, it is associated with a strong enhancement of the RF sheath voltage near conditions of sheath-plasma resonance.[18-21,32,33]

IV. CONCLUSIONS

In this paper, we have studied the interactions between propagating FWs and RF sheaths in a non-circular poloidal cross-section of a tokamak under conditions similar to those in Alcator C-Mod tokamak experiments. The parameters were chosen such that SWs are always evanescent in the plasma. The main result of the paper is the observation of "far-field" sheaths generated by the FW-to-SW conversion process in a tokamak-like geometry, and the dependencies of such sheath on important parameters. To our knowledge, this is the first time that far-field sheaths have been demonstrated in a global ICRF code employing sheath BCs

and non-trivial geometry.

The study here highlights the enhancement of the sheath voltage due to the FW-to-SW conversion, which occurs when the contact angle between the magnetic field line and the conducting wall varies rapidly within a small length scale. The larger the degree of mismatch of the wall shape with flux surfaces and the rate of change of the contact angle, the larger the localized sheath voltage due to generation of a large electric field component parallel to the background magnetic field; then, at some point the sheath voltage grows much faster than the increase in the parallel electric field component due to the nonlinearity of the sheath width.

Through this conversion process, it was demonstrated in the present numerical analysis that a sheath voltage of more than 100 V can be generated from a propagating FW with a field strength of a few kV/m. Considering that the inner wall areas of real tokamaks are not entirely flat due to the protrusion of hardware, there is a possibility that we could observe a relatively wide range of spots of high sheath voltage even far from the location of the antenna. The existence of large plasma potentials on surfaces not magnetically connected to the antennas due to fast waves encountering walls and limiters has been observed on Alcator C-Mod.[13] This effect could be especially important for the start-up scenario of the ITER experiments where central absorption is expected, under standard ICRF scenarios, to be poor in association with the operation at half the nominal magnetic field strength.

In addition, the dependences of the RF sheaths on the toroidal wavenumber and the edge plasma density were also investigated. It was demonstrated in both cases that the variation in the propagation characteristics of fast and slow waves in plasma plays an important role in the increase or decrease of the local sheath voltage. For large values of the toroidal wavenumber, the sheath voltage generated through the FW-to-SW conversion was largely decreased due to the evanescence of FWs in the boundary region. On the other hand, another type of sheath emerged when decreasing the edge plasma density; this is called the direct magnetically connected sheath, which is formed by the interaction of a SW with the conducting wall. Even though a SW generated from the antenna is evanescent in the present analysis, the rate of SW evanescence becomes lower for smaller plasma density (but larger than lower hybrid plasma density). Thus, a relatively large electric field component parallel to the background magnetic field can still reach the boundary region. As a result, it was shown that the sheath voltage generated by this SW-sheath interaction becomes higher than that generated by the FW-to-SW conversion for a sufficiently small edge plasma density value.

The next step in the development of the finite element code will be improvement of the sheath BC model by adding the sheath dissipation for which a nonlinear relation might need to be solved self-consistently. Once this implementation is successfully achieved, it is hoped that we can calculate the power density on “hot spots,” which is important to assess the

possibility of material damage.

ACKNOWLEDGMENTS

Discussions with the rf-SciDAC team (Center for Simulation of Wave-Plasma Interactions) are gratefully acknowledged. This material is based upon work supported by the U.S. Department of Energy Office of Science, Office of Fusion Energy Sciences, under Award Number DE-FC02-05ER54823. This research used resources of the National Energy Research Scientific Computing Center, a DOE Office of Science User Facility supported by the Office of Science of the U.S. Department of Energy under Contract No. DE-AC02-05CH11231.

APPENDIX A: RF DIELECTRIC RESPONSE WITH FRICTION

In this appendix, we briefly demonstrate how the addition of the ad-hoc friction modifies the dielectric response, especially for the FW ICRF branch. First, the system of equations that must be solved takes the form of Maxwell's equations (see Eq. (1)) and the species momentum equation described as

$$-\mathrm{i}\omega m_j \mathbf{v}_j = Z_j e\left(\mathbf{E} + \mathbf{v}_j \times \mathbf{B}\right) - m_j \nu\, \mathbf{v}_j, \tag{A1}$$

where the subscript j denotes ion (i) or electron (e), m_j is the mass, $\mathbf{v}_j$ is the flow velocity, Z_j is the charge number of the species j, and ν is the rate of frictional dissipation. A short calculation reveals that this friction formulation is equivalent to the complex mass formulation in which a complex mass is defined in the form $m_j \to m_j(1+\mathrm{i}\alpha)$ with $\nu = 0$; and then, we identify $\nu = \omega\alpha$. Assuming a Fourier mode in space in Eq. (1), the FW dispersion relation is given by

$$\left(\varepsilon_\perp - n_\parallel^2\right)\left(\varepsilon_\perp - n^2\right) = \varepsilon_\times^2, \tag{A2}$$

where $n_\parallel = \mathbf{n}\cdot\mathbf{b}$ and $n^2 = \mathbf{n}\cdot\mathbf{n}$, and $\mathbf{n}$ is the index of refraction. Summing over species, dropping ν for the electrons but retaining it for the ions, and taking $Z_\mathrm{i} = 1$, the dielectric tensor components in Eq. (A2) are expressed as follows:

$$\varepsilon_\perp = 1 + \frac{\omega_\mathrm{pe}^2}{\Omega_\mathrm{e}^2} - \frac{\omega_\mathrm{pi}^2\hat{\omega}}{\omega\left(\hat{\omega}^2 - \Omega_\mathrm{i}^2\right)}, \qquad \varepsilon_\times = \frac{\omega_\mathrm{pi}^2\hat{\omega}^2}{\omega\Omega_\mathrm{i}\left(\hat{\omega}^2 - \Omega_\mathrm{i}^2\right)}, \tag{A3}$$

where $\omega_{\mathrm{p}j}$ is the plasma frequency defined as $\omega_{\mathrm{p}j} = \left(n_j e^2/\varepsilon_0 m_j\right)^{1/2}$, $\Omega_j = Z_j eB_0/m_j$ (again, j denotes i or e), and $\hat{\omega} = \omega + \mathrm{i}\nu$. Note that the expressions in Eq. (A3) are valid for the ICRF. From Eqs. (A2) and (A3), we conclude that the FWs are strongly damped spatially in the cold fluid plasma model when $\omega \sim \nu$, i.e., ion friction is effective for FW damping. Conversely, it is straightforward to show that electron friction, or equivalently complex electron mass (not retained in Eq. (A3)), is ineffective in damping the ICRF FW; for $\Omega_\mathrm{e} >> \omega \sim \nu$, both friction and inertia are unimportant in the electron momentum equation.

APPENDIX B: ACCURACY IMPROVEMENT OF THE FINITE ELEMENT CODE

In the previous version of the rfSOL code, the integrals appearing in the discretized Maxwell's equation are approximately calculated by applying the element average to the Jacobian and contravariant base vectors in each nine-node element (see Ref. 42). This approximation is efficient only if a small amount of grid distortion is retained everywhere in the calculation domain; therefore, this method works well for the analysis of sheath-plasma interactions in a slab domain since all the quadrilateral nine-node elements can be rectangular. In the present numerical analysis, a large amount of grid distortion can locally occur as seen in Fig. 1(b), and thus, the element-average technique used in our previous work should cause a significant error in the numerical solution. For that reason, all the integrals in the discretized Maxwell's equation are numerically calculated in this study using the three-point Gaussian quadrature rule for the integrations with respect to ξ and η ($-1 \le \xi, \eta \le 1$). It has been confirmed that the modified rfSOL code is robust with respect to various kinds of grid distortion in the quasi-circular domain.

The integrals which appear in the discretized sheath BC are also strictly calculated without the use of the element-average technique described in Ref. 37. To demonstrate this, the discretization procedure for the sheath BC is reviewed below. First of all, the sheath BC

shown in Eq. (2) is rewritten as follows:

$$\mathbf{E}_{\mathrm{t}} = \nabla_{\mathrm{t}}\left(\mathbf{s}\cdot\boldsymbol{\chi}\cdot\mathbf{E}\right), \tag{B1}$$

where

$$\begin{aligned} &\boldsymbol{\chi} = \left(\alpha_{\mathrm{sh}}\left|\kappa\right|^3 + \beta_{\mathrm{sh}}\right)\boldsymbol{\varepsilon}, \\ &\alpha_{\mathrm{sh}} = \left(\frac{eC_{\mathrm{sh}}}{T_{\mathrm{e}}}\right)^3 \lambda_{\mathrm{De}}^4, \quad \beta_{\mathrm{sh}} = C_{\mathrm{th}}\lambda_{\mathrm{De}}, \quad \kappa = \mathbf{s}\cdot\boldsymbol{\varepsilon}\cdot\mathbf{E}. \end{aligned} \tag{B2}$$

Note that α_{sh} and β_{sh} are functions of τ (the tangential direction with respect to the sheath surface and perpendicular to the z direction) since λ_{De} and C_{th} vary along the sheath surface. Forming the inner product of Eq. (B1) with the weight function $\mathbf{W}^{\mathrm{S}}$, and then integrating it over the sheath region Γ^{S} yields

$$\int_{\Gamma^{\mathrm{S}}} \mathbf{W}^{\mathrm{S}}\cdot\left[\mathbf{E}_{\mathrm{t}} - \nabla_{\mathrm{t}}\left(\mathbf{s}\cdot\boldsymbol{\chi}\cdot\mathbf{E}\right)\right]\mathrm{d}\Gamma^{\mathrm{S}} = 0. \tag{B3}$$

In the present numerical analysis, the weight function and electric field are, respectively, defined as

$$\mathbf{W}^{\mathrm{S}} = \hat{\mathbf{W}}_i^{\mathrm{S}} N_i^{\mathrm{S}}(\tau)\mathrm{e}^{-\mathrm{i}k_z z} = \hat{\mathbf{W}}_i^{\mathrm{S}}\widetilde{N}_i^{\mathrm{S}}, \tag{B4}$$

$$\mathbf{E} = \hat{\mathbf{E}}_j^{\mathrm{S}} N_j^{\mathrm{S}}(\tau)\mathrm{e}^{\mathrm{i}(k_z z-\omega t)}, \tag{B5}$$

where N_i^{S} and N_j^{S} are the piecewise quadratic interpolation functions with respect to τ, and the subscripts i and j denote the global node number on the domain of the surface Γ^{S}. Here the summation convention applies to the subscripts i and j, and the superscript S is attached to explicitly show that the quantity is positioned on Γ^{S}. Considering that Eq. (B3)

needs to be satisfied for arbitrary weight functions, one gets

$$\int_{\Gamma^{\mathrm{S}}} \widetilde{N}_i^{\mathrm{S}} \left[\mathbf{E}_{\mathrm{t}} - \nabla_{\mathrm{t}} \left(\mathbf{s} \cdot \boldsymbol{\chi} \cdot \mathbf{E} \right) \right] \mathrm{d}\Gamma^{\mathrm{S}} = \mathbf{0}. \tag{B6}$$

Let us consider the discretization of the τ component of Eq. (B6), i.e.,

$$\int_{\Gamma^{\mathrm{S}}} \widetilde{N}_i^{\mathrm{S}} \left[E_\tau - \frac{\partial}{\partial \tau} \left(\mathbf{s} \cdot \boldsymbol{\chi} \cdot \mathbf{E} \right) \right] \mathrm{d}\Gamma^{\mathrm{S}} = 0. \tag{B7}$$

Assuming that $\mathbf{s}$ and $\boldsymbol{\chi}$ are interpolated as $\mathbf{s} = N_k^{\mathrm{S}} \mathbf{s}_k$ and $\boldsymbol{\chi} = N_l^{\mathrm{S}} \boldsymbol{\chi}_l^{\mathrm{S}}$, respectively, using their nodal values $\mathbf{s}_k$ and $\boldsymbol{\chi}_l^{\mathrm{S}}$, and substituting Eq. (B5) into Eq. (B7), we obtain

$$G_{\tilde{\imath}} \equiv \left[N_i^{\mathrm{S}} N_j^{\mathrm{S}} \right] \hat{E}_{\tilde{\jmath}}^{\mathrm{S}} - \left[N_i^{\mathrm{S}} \breve{N}_j^{\mathrm{S}} \breve{N}_k^{\mathrm{S}} \breve{N}_l^{\mathrm{S}} \right] \mathbf{s}_k \cdot \boldsymbol{\chi}_l^{\mathrm{S}} \cdot \hat{\mathbf{E}}_j^{\mathrm{S}} = 0, \tag{B8}$$

with

$$\begin{aligned} \left[N_i^{\mathrm{S}} N_j^{\mathrm{S}} \right] &\equiv \int_{\Gamma^{\mathrm{S}}} N_i^{\mathrm{S}} N_j^{\mathrm{S}} \mathrm{d}\Gamma^{\mathrm{S}}, \\ \left[N_i^{\mathrm{S}} \breve{N}_j^{\mathrm{S}} \breve{N}_k^{\mathrm{S}} \breve{N}_l^{\mathrm{S}} \right] &\equiv \int_{\Gamma^{\mathrm{S}}} N_i^{\mathrm{S}} \frac{\mathrm{d}}{\mathrm{d}\tau} \left(N_j^{\mathrm{S}} N_k^{\mathrm{S}} N_l^{\mathrm{S}} \right) \mathrm{d}\Gamma^{\mathrm{S}}. \end{aligned} \tag{B9}$$

The integrals in Eq. (B9) are rigorously calculated without the use of a numerical integration method. The quantity $\hat{E}_{\tilde{\jmath}}^{\mathrm{S}}$ needs to be expressed using $\hat{E}_{xj}^{\mathrm{S}}$ and $\hat{E}_{yj}^{\mathrm{S}}$ as

$$\hat{E}_{\tilde{\jmath}}^{\mathrm{S}} = \mathbf{e}_x \cdot \mathbf{e}_{\tilde{\jmath}} \hat{E}_{xj}^{\mathrm{S}} + \mathbf{e}_y \cdot \mathbf{e}_{\tilde{\jmath}} \hat{E}_{yj}^{\mathrm{S}}, \tag{B10}$$

where $\mathbf{e}_{\tilde{\jmath}}$ is the unit vector in the τ direction at the node j. Then the expression of $G_{\tilde{\imath}}$ is easily divided into real and imaginary parts as follows:

$$\begin{aligned} G_{\tilde{\imath}}^{(\mathrm{R})} &\equiv \left[N_i^{\mathrm{S}} N_j^{\mathrm{S}} \right] \left(\mathbf{e}_x \cdot \mathbf{e}_{\tilde{\jmath}} \hat{E}_{xj}^{\mathrm{S(R)}} + \mathbf{e}_y \cdot \mathbf{e}_{\tilde{\jmath}} \hat{E}_{yj}^{\mathrm{S(R)}} \right) - \left[N_i^{\mathrm{S}} \breve{N}_j^{\mathrm{S}} \breve{N}_k^{\mathrm{S}} \breve{N}_l^{\mathrm{S}} \right] \mathbf{s}_k \cdot \mathrm{Re}\left(\boldsymbol{\chi}_l^{\mathrm{S}} \cdot \hat{\mathbf{E}}_j^{\mathrm{S}} \right) = 0, \\ G_{\tilde{\imath}}^{(\mathrm{I})} &\equiv \left[N_i^{\mathrm{S}} N_j^{\mathrm{S}} \right] \left(\mathbf{e}_x \cdot \mathbf{e}_{\tilde{\jmath}} \hat{E}_{xj}^{\mathrm{S(I)}} + \mathbf{e}_y \cdot \mathbf{e}_{\tilde{\jmath}} \hat{E}_{yj}^{\mathrm{S(I)}} \right) - \left[N_i^{\mathrm{S}} \breve{N}_j^{\mathrm{S}} \breve{N}_k^{\mathrm{S}} \breve{N}_l^{\mathrm{S}} \right] \mathbf{s}_k \cdot \mathrm{Im}\left(\boldsymbol{\chi}_l^{\mathrm{S}} \cdot \hat{\mathbf{E}}_j^{\mathrm{S}} \right) = 0, \end{aligned} \tag{B11}$$

where the superscripts R and I denote the real and imaginary parts of the quantity, respectively. In the rfSOL code, a Newton-Raphson method is employed to solve the nonlinear system of

the discretized equations. Therefore, the derivative expressions of the discretized sheath BC with respect to the nodal values of the electric field components are required. For example, the derivative expression of $G_{\tilde{n}}^{(\mathrm{R})}$ with respect to $\hat{E}_{xm}^{\mathrm{S(R)}}$ (where the subscript m denotes the global node number) is given by

$$\begin{aligned}\frac{\partial G_{\tilde{n}}^{(\mathrm{R})}}{\partial \hat{E}_{xm}^{\mathrm{S(R)}}} &= \left[N_i^{\mathrm{S}} N_m^{\mathrm{S}}\right]\mathbf{e}_x \cdot \mathbf{e}_{\tilde{n}m} - \left[N_i^{\mathrm{S}} \breve{N}_j^{\mathrm{S}} \breve{N}_k^{\mathrm{S}} \breve{N}_m^{\mathrm{S}}\right] T_{xm}^{(\mathrm{R})} \mathbf{s}_k \cdot \mathrm{Re}\left(\boldsymbol{\varepsilon}_m^{\mathrm{S}} \cdot \hat{\mathbf{E}}_j^{\mathrm{S}}\right) \\ &\quad - \left[N_i^{\mathrm{S}} \breve{N}_m^{\mathrm{S}} \breve{N}_k^{\mathrm{S}} \breve{N}_l^{\mathrm{S}}\right]\left(s_{xk}\chi_{xxl}^{\mathrm{S(R)}} + s_{yk}\chi_{yxl}^{\mathrm{S(R)}}\right),\end{aligned} \tag{B12}$$

where

$$\begin{aligned}T_{xm}^{(\mathrm{R})} &= 3\alpha_{\mathrm{sh},m}\left|\hat{\kappa}_m\right|\left[\hat{\kappa}_m^{(\mathrm{R})}\left(s_{xm}\varepsilon_{xxm}^{\mathrm{S(R)}} + s_{ym}\varepsilon_{yxm}^{\mathrm{S(R)}}\right) + \hat{\kappa}_m^{(\mathrm{I})}\left(s_{xm}\varepsilon_{xxm}^{\mathrm{S(I)}} + s_{ym}\varepsilon_{yxm}^{\mathrm{S(I)}}\right)\right], \\ \hat{\kappa}_m &= \mathbf{s}_m \cdot \boldsymbol{\varepsilon}_m^{\mathrm{S}} \cdot \hat{\mathbf{E}}_m^{\mathrm{S}}.\end{aligned} \tag{B13}$$

Note that the summation convention does not apply to the subscript m, and the relation between $\boldsymbol{\chi}_m^{\mathrm{S}}$ and $\boldsymbol{\varepsilon}_m^{\mathrm{S}}$, i.e.,

$$\boldsymbol{\chi}_m^{\mathrm{S}} = \left(\alpha_{\mathrm{sh},m}\left|\kappa_m\right|^3 + \beta_{\mathrm{sh},m}\right)\boldsymbol{\varepsilon}_m^{\mathrm{S}} \tag{B14}$$

is employed to obtain Eq. (B12). Following the same procedure, one can obtain the derivative expressions of $G_{\tilde{n}}^{(\mathrm{R})}$ with respect to the other real and imaginary parts of the electric field components, and the derivatives of $G_{\tilde{n}}^{(\mathrm{I})}$. Although not shown in this appendix, one can also carry out the discretization of the z component of Eq. (B6) and obtain its derivative expressions by following the procedure described above.

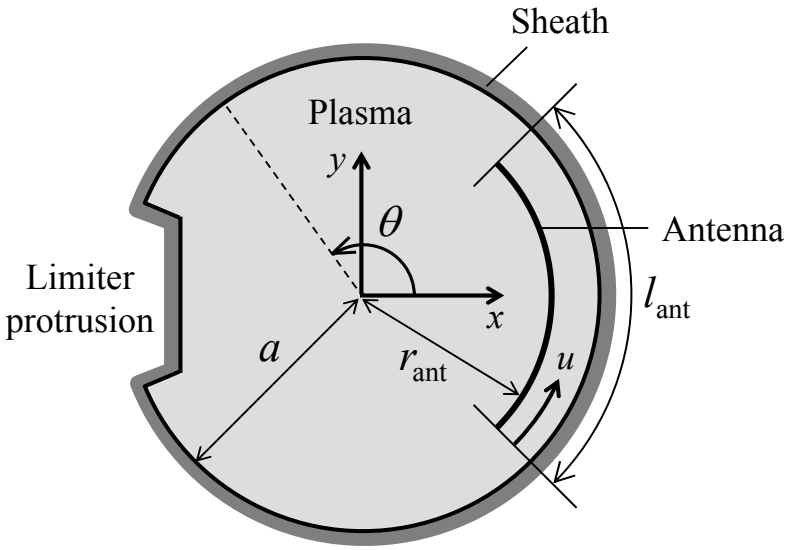

(a)

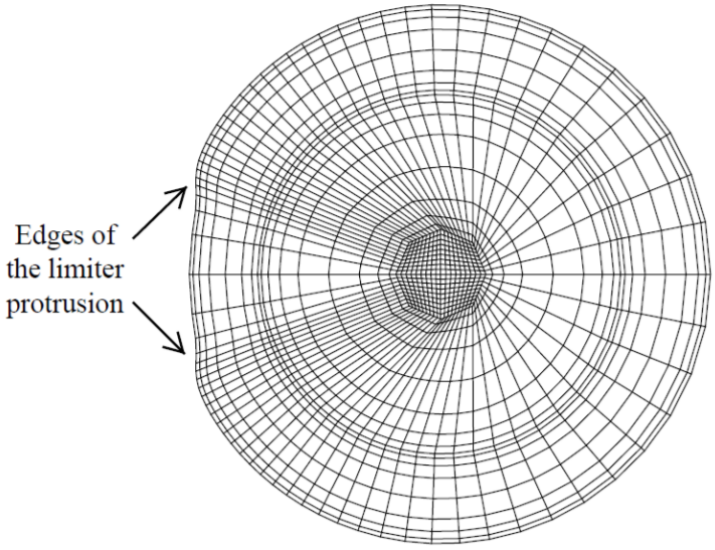

(b)

FIG. 1. Geometry of the calculation domain and the mesh used: (a) problem definition; and (b) variable mesh which consists of nine-node elements. The geometry corresponds approximately to the poloidal cross-section of a tokamak.

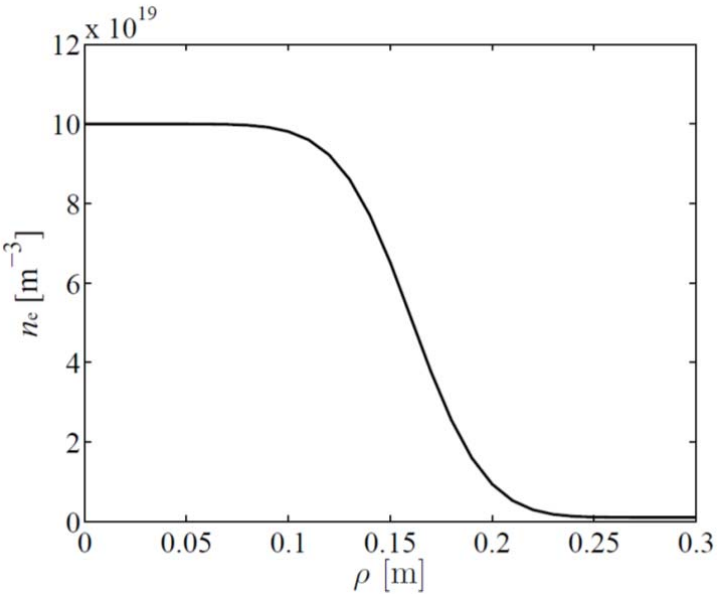

FIG. 2. The electron density profile for $n_e|_{\Psi_p=\infty} = 10^{18}\ \mathrm{m}^{-3}$ as a function of ρ.

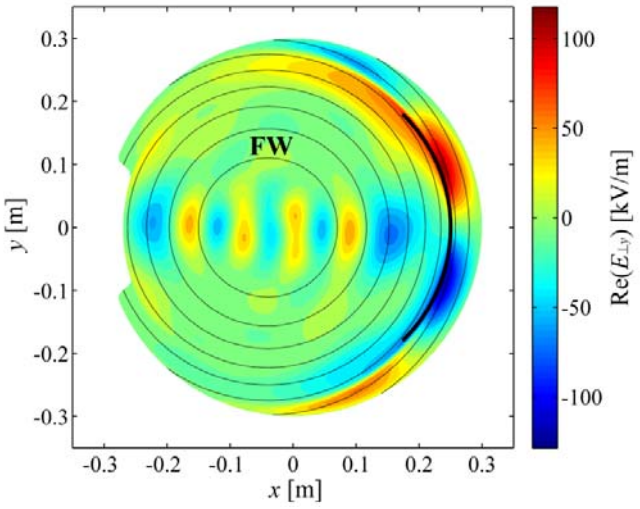

(a)

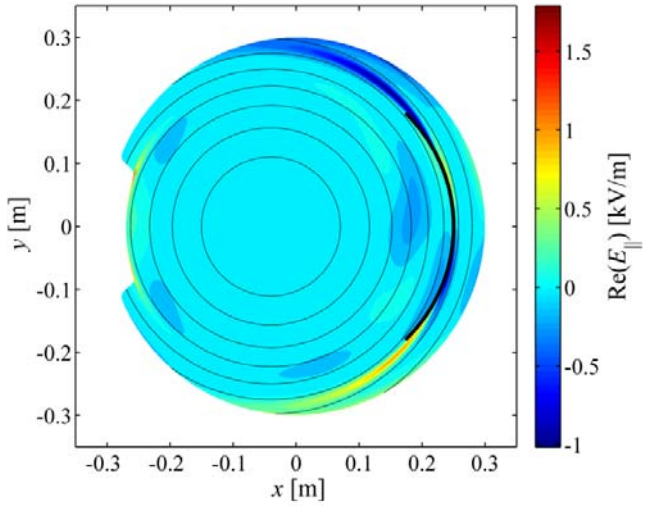

(b)

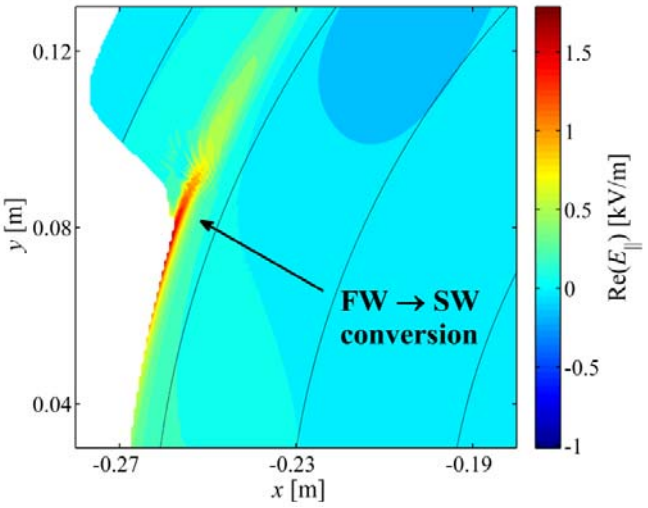

(c)

FIG. 3. (Color online) Filled contour plots of $\mathrm{Re}(E_{\perp y})$ (a), $\mathrm{Re}(E_{\parallel})$ (b) and its expanded view near the edge of the limiter protrusion (c) for the base case. Note that the FW-to-SW conversion occurs where $|b_{\mathrm{n}}|$ changes rapidly.

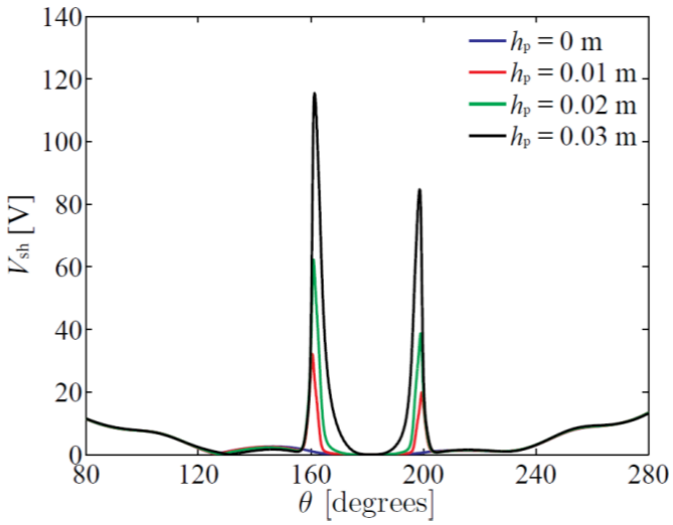

(a)

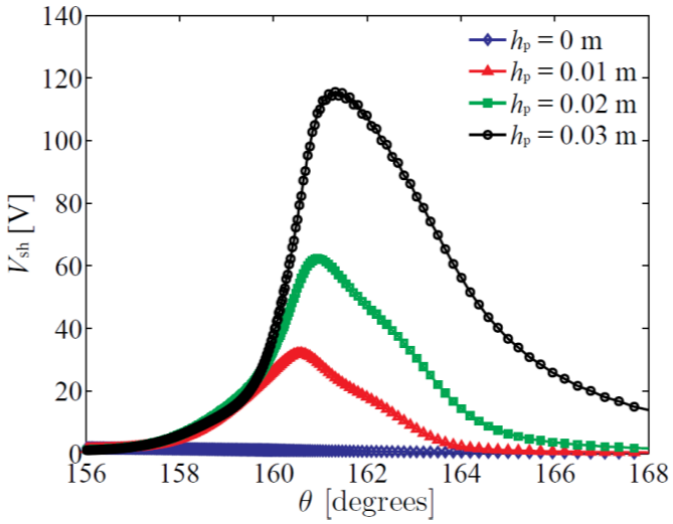

(b)

FIG. 4. (Color online) Instantaneous RF sheath voltage V_{sh} vs. the poloidal angle θ for four different heights of the limiter protrusion: (a) wide-range profiles; and (b) localized profiles at the edge of the limiter. The peak sheath voltage of about 115 V occurs for the case where $h_p = 0.03$ m (the base case) and decreases monotonically with decrease in h_p.

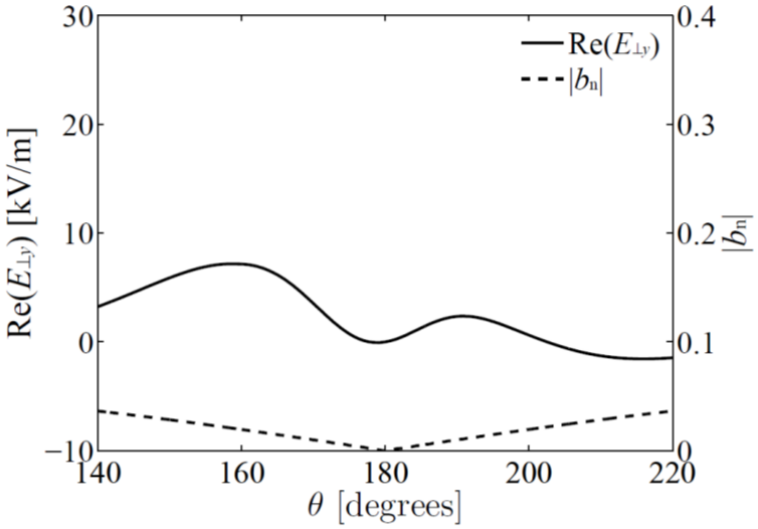

(a)

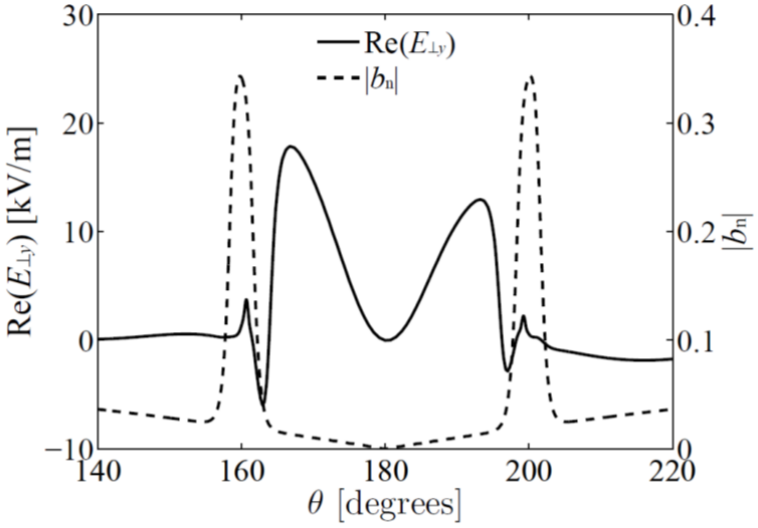

(b)

FIG. 5. Plots of the real part of $E_{\perp y}$ and $|b_n|$ as functions of the poloidal angle θ for $h_p = 0$ m (a) and $h_p = 0.03$ m (the base case) (b).

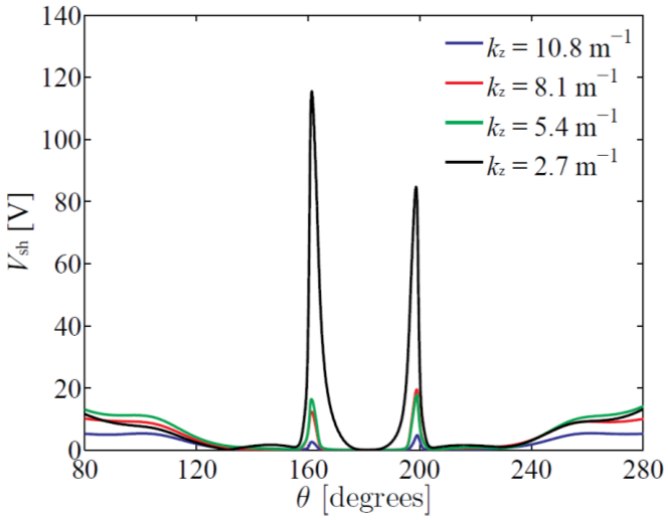

(a)

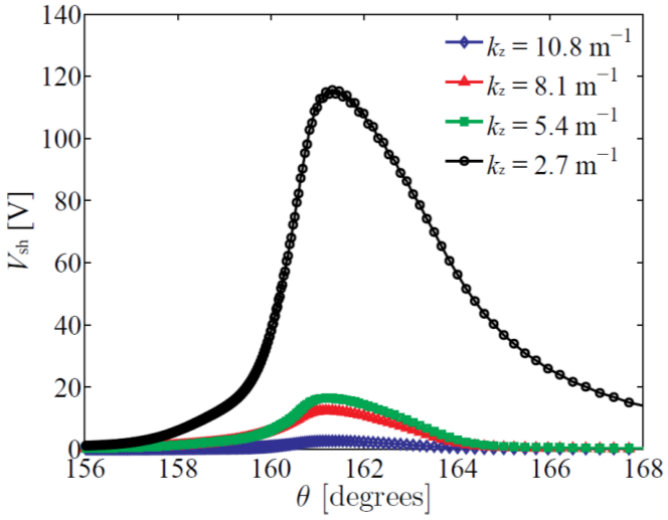

(b)

FIG. 6. (Color online) Instantaneous RF sheath voltage V_{sh} vs. the poloidal angle θ for four different values of k_z: (a) wide-range profiles; and (b) localized profiles at the edge of the limiter. The peak sheath voltage of about 115 V occurs for the case where $k_z = 2.7\ \mathrm{m}^{-1}$ (the base case) and decreases with increase in k_z.

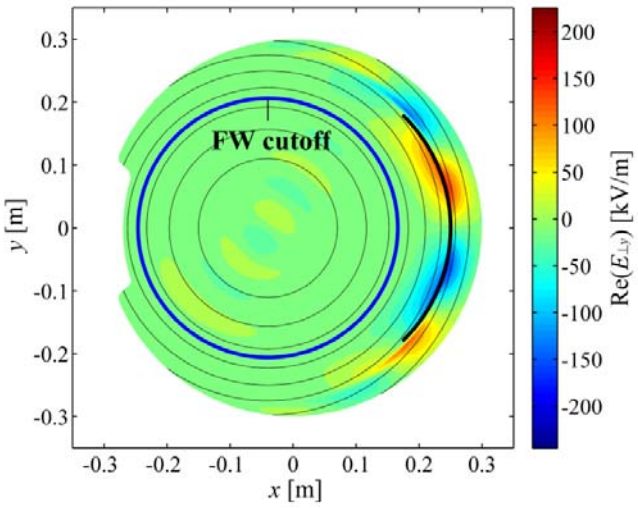

FIG. 7. (Color online) Filled contour plot of $\mathrm{Re}\left(E_{\perp y}\right)$ for the case of $k_z = 10.8\,\mathrm{m}^{-1}$. Here, the blue line denotes the FW cutoff. Notice that the FW evanescent electric fields do not reach the limiter protrusion.

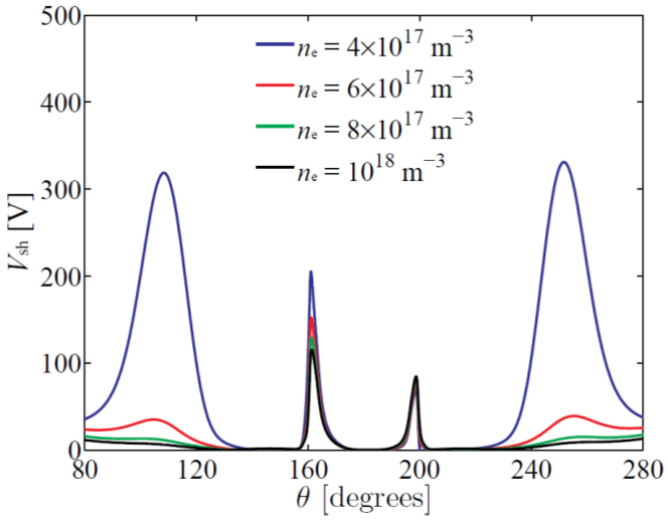

(a)

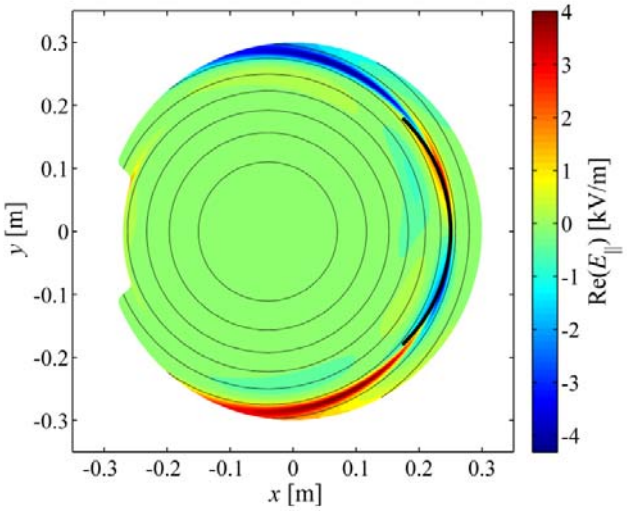

(b)

FIG. 8. (Color online) (a) Instantaneous RF sheath voltage V_{sh} vs. the poloidal angle θ for four different values of the edge plasma density $n_e|_{\Psi_p=\infty}$; and (b) filled contour plot of $\mathrm{Re}(E_\parallel)$ for the case of $n_e|_{\Psi_p=\infty} = 4\times10^{17}$ m^{-3}. The peak sheath voltage of about 330 V occurs for the case where $n_e|_{\Psi_p=\infty} = 4\times10^{17}$ m^{-3} and decreases with increase in $n_e|_{\Psi_p=\infty}$.

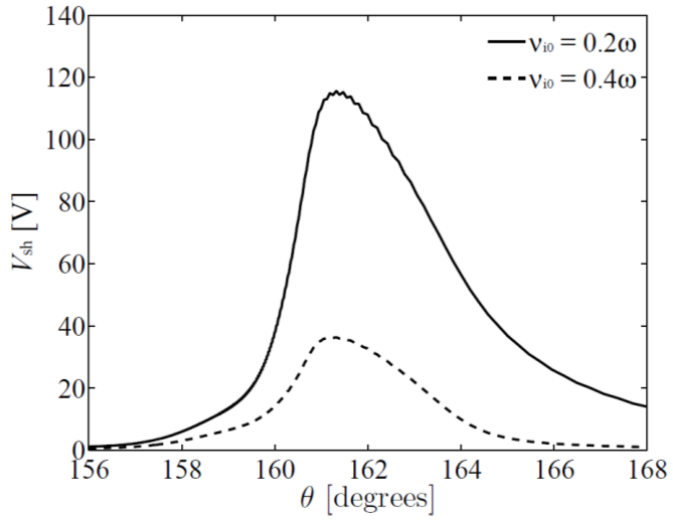

(a)

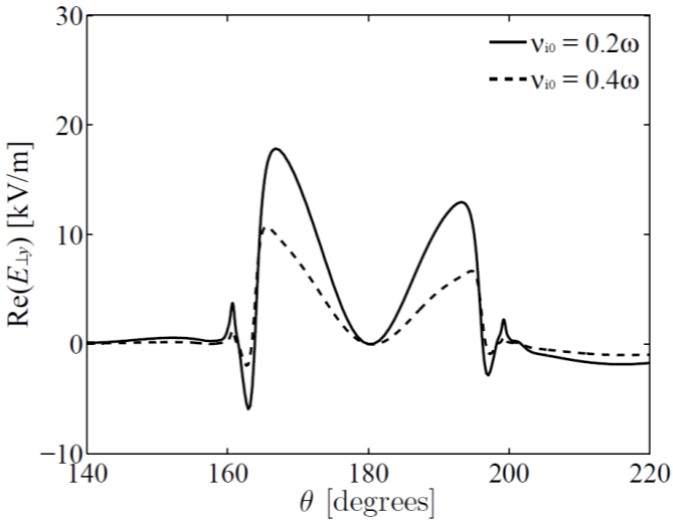

(b)

FIG. 9. Comparison of the instantaneous RF sheath voltage V_{sh} (a) and the real part of $E_{\perp y}$ (b) as functions of the poloidal angle θ along the sheath surface between the cases of $\nu_{i0} = 0.2\omega$ (the base case) and $\nu_{i0} = 0.4\omega$.

References

[1] J. R. Wilson and P. T. Bonoli, Phys. Plasmas **22**, 021801 (2015).

[2] J.-M. Noterdaeme and G. Van Oost, Plasma Phys. Controlled Fusion **35**, 1481 (1993).

[3] J. R. Myra, D. A. D'Ippolito, D. A. Russell, L. A. Berry, E. F. Jaeger, and M. D. Carter, Nucl. Fusion **46**, S455 (2006).

[4] D. A. D'Ippolito and J. R. Myra, J. Nucl. Mater. **415**, S1001 (2011).

[5] S. J. Wukitch, M. L. Garrett, R. Ochoukov, J. L. Terry, A. Hubbard, B. Labombard, C. Lau, Y. Lin, B. Lipschultz, D. Miller, M. L. Reinke, D. Whyte, and Alcator C-Mod Team, Phys. Plasmas **20**, 056117 (2013).

[6] V. Bobkov, M. Balden, R. Bilato, F. Braun, R. Dux, A. Herrmann, H. Faugel, H. Fünfgelder, L. Giannone, A. Kallenbach, H. Maier, H. W. Müller, R. Neu, J.-M. Noterdaeme, Th. Pütterich, V. Rohde, N. Tsujii, F. Zeus, H. Zohm, and the ASDEX Upgrade Team, Nucl. Fusion **53**, 093018 (2013).

[7] J. Jacquot, D. Milanesio, L. Colas, Y. Corre, M. Goniche, J. Gunn, S. Heuraux, and M. Kubič, Phys. Plasmas **21**, 061509 (2014).

[8] C. M. Qin, Y. P. Zhao, H. Q. Wang, X. J. Zhang, B. N. Wan, J.-M. Noterdaeme, F. Braun, V. Bobkov, H. Kasahara, E. H. Kong, L. Wang, Y. Shuai, Z. X. He, B. J. Ding, ICRF Team and EAST Team, Plasma Phys. Controlled Fusion **55**, 015004 (2013).

[9] Y. Corre, M. Firdaouss, L. Colas, A. Argouarch, D. Guilhem, J. Gunn, C Hamlyn-Harris, J. Jacquot, M. Kubic, X. Litaudon, M. Missirlian, M. Richou, G. Ritz, D. Serret, and K. Vulliez, Nucl. Fusion **52**, 103010 (2012).

[10] I. Cziegler, J. L. Terry, S. J. Wukitch, M. L. Garrett, C. Lau, and Y. Lin, Plasma Phys. Controlled Fusion **54**, 105019 (2012).

[11] R. J. Perkins, J.-W. Ahn, R. E. Bell, A. Diallo, S. Gerhardt, T. K. Gray, D. L. Green, E. F. Jaeger, J. C. Hosea, M. A. Jaworski, B. P. LeBlanc, G. J. Kramer, A. McLean, R. Maingi, C. K. Phillips, M. Podestà, L. Roquemore, P. M. Ryan, S. Sabbagh, F. Scotti, G. Taylor, and J. R. Wilson, Nucl. Fusion **53**, 083025 (2013).

[12] P. Jacquet, L. Colas, M.-L. Mayoral, G. Arnoux, V. Bobkov, M. Brix, P. Coad, A. Czarnecka, D. Dodt, F. Durodie, A. Ekedahl, D. Frigione, M. Fursdon, E. Gauthier, M. Goniche, M. Graham, E. Joffrin, A. Korotkov, E. Lerche, J. Mailloux, I. Monakhov, C. Noble, J. Ongena, V. Petrzilka, C. Portafaix, F. Rimini, A. Sirinelli, V. Riccardo, Z. Vizvary, A. Widdowson, K.-D. Zastrow, and JET EFDA Contributors, Nucl. Fusion **51**, 103018 (2011).

[13] R. Ochoukov, D. G. Whyte, D. Brunner, D. A. D'Ippolito, B. LaBombard, B. Lipschultz, J. R. Myra, J. L. Terry, and S. J. Wukitch, Plasma Phys. Controlled Fusion **56**, 015004 (2014).

[14] L. Colas, J. Jacquot, S. Heuraux, E. Faudot, K. Crombé, V. Kyrytsya, J. Hillairet, and M. Goniche, Phys. Plasmas **19**, 092505 (2012).

[15] D. N. Smithe, D. A. D'Ippolito, and J. R. Myra, *AIP Conference Proceedings* **1580**, 89 (2014).

[16] N. Bertelli, E. F. Jaeger, J. C. Hosea, C. K. Phillips, L. Berry, S. P. Gerhardt, D. Green, B. LeBlanc, R. J. Perkins, P. M. Ryan, G. Taylor, E. J. Valeo, and J. R. Wilson, Nucl. Fusion **54**, 083004 (2014).

[17] D. Van Eester, K. Crombé, and V. Kyrytsya, Plasma Phys. Controlled Fusion **55**, 055001 (2013).

[18] J. R. Myra and D. A. D'Ippolito, Plasma Phys. Controlled Fusion **52**, 015003 (2010).

[19] H. Kohno, J. R. Myra, and D. A. D'Ippolito, Phys. Plasmas **19**, 012508 (2012).

[20] D. A. D'Ippolito, J. R. Myra, R. Ochoukov, and D. G. Whyte, Plasma Phys. Controlled Fusion **55**, 085001 (2013).

[21] H. Kohno, J. R. Myra, and D. A. D'Ippolito, Phys. Plasmas **20**, 082514 (2013).

[22] F. W. Perkins, Nucl. Fusion **29**, 583 (1989).

[23] J. R. Myra, D. A. D'Ippolito, and M. J. Gerver, Nucl. Fusion **30**, 845 (1990).

[24] M. Brambilla, R. Chodura , J. Hoffmann and J. Neuhauser, *Proceedings of the 13th International Conference on Plasma Physics and Controlled Nuclear Fusion Research* (Washington, D.C., 1990) Vol.1 (International Atomic Energy Agency, Vienna, 1991), p.723.

[25] J. R. Myra, D. A. D'Ippolito, and Y. L. Ho, Fusion Eng. Des. **31**, 291 (1996).

[26] D. A. D'Ippolito, J. R. Myra, J. H. Rogers, K. W. Hill, J. C. Hosea, R. Majeski, G. Schilling, J. R. Wilson, G. R. Hanson, A. C. England, and J. B. Wilgen, Nucl. Fusion **38**, 1543 (1998).

[27] M. Bécoulet, L. Colas, S. Pécoul, J. Gunn, Ph. Ghendrih, A. Bécoulet, and S. Heuraux, Phys. Plasmas **9**, 2619 (2002).

[28] K. Crombé, V. Kyrytsya, R. Koch, and D. Van Eester, *AIP Conference Proceedings* **1406**, 97 (2011).

[29] J. Hosea, R. E. Bell, B. P. LeBlanc, C. K. Phillips, G. Taylor, E. Valeo, J. R. Wilson, E. F. Jaeger, P. M. Ryan, J. Wilgen, H. Yuh, F. Levinton, S. Sabbagh, K. Tritz, J. Parker, P. T. Bonoli, R. Harvey, and NSTX Team, Phys. Plasmas **15**, 056104 (2008).

[30] C. C. Petty, R. I. Pinsker, M. E. Austin, F. W. Baity, S. C. Chiu, J. S. DeGrassie, C. B. Forest, R. H. Goulding, R. W. Harvey, D. J. Hoffman, R. A. James, T. C. Luce, M. Porkolab, and R. Prater, Nucl. Fusion **35**, 773 (1995).

[31] J. R. Myra, D. A. D'Ippolito, and M. Bures, Phys. Plasmas **1**, 2890 (1994).

[32] D. A. D'Ippolito, J. R. Myra, E. F. Jaeger, and L. A. Berry, Phys. Plasmas **15**, 102501 (2008).

[33] D. A. D'Ippolito and J. R. Myra, Phys. Plasmas **13**, 102508 (2006).

[34] T. H. Stix, *Waves in Plasmas*, American Institute of Physics (1992).

[35] C. D. Child, Phys. Rev. (Series I) **32**, 492 (1911).

[36] I. Langmuir, Phys. Rev. **21**, 419 (1923).

[37] H. Kohno, J. R. Myra, and D. A. D'Ippolito, Comput. Phys. Commun. **183**, 2116 (2012).

[38] D. F. H. Start, G. Bell, V. P. Bhatnagar, M. Bures, G. A. Cottrell, L.-G. Eriksson, B. Fechner, R. Goulding, C. Gormezano, A. Howman, J. Jacquinot, A. Kaye, P. Lamalle, F. Nguyen, E. Righi, F. Rimini, A. Sibley, A. C. C. Sips, B. J. Tubbing, T. Wade, and D. Ward, *Proceedings of the 11th Topical Conference on Radio Frequency Power in Plasmas* (Palm Springs, California, 1995) Vol. 355 (American Institute of Physics, Melville, 1995), p.7.

[39] T. Hellsten, M. Laxåback, T. Bergkvist, T. Johnson, F. Meo, F. Nguyen, C. C. Petty, M. Mantsinen, G. Matthews, J.-M. Noterdaeme, T. Tala, D. Van Eester, P. Andrew, P. Beaumont, V. Bobkov, M. Brix, J. Brzozowski, L.-G. Eriksson, C. Giroud, E. Joffrin, V. Kiptily, J. Mailloux, M.-L. Mayoral, I. Monakhov, R. Sartori, A. Staebler, E. Rachlew, E. Tennfors, A. Tuccillo, A. Walden, K.-D. Zastrow, and JET-EFDA Contributors, Nucl. Fusion **45**, 706 (2005).

[40] J. E. Stevens, C. Bush, P. L. Colestock, G. J. Greene, K. W. Hill, J. C. Hosea, C. K. Phillips, B. Stratton, S. von Goeler, J. R. Wilson, W. Gardner, D. Hoffman, and A. Lysojvan, Plasma Phys. Controlled Fusion **32**, 189 (1990).

[41] M. Bureš, J. Jacquinot, K. Lawson, M. Stamp, H. P. Summers, D. A. D'Ippolito, and J. R. Myra, Plasma Phys. Controlled Fusion **33**, 937 (1991).
[42] H. Kohno, "Numerical analysis of radio-frequency sheath-plasma interactions in the ion cyclotron range of frequencies," Sc.D. thesis, MIT, 2011.